

Direct measurement of the plasma loss width in an optimized, high ionization fraction, magnetic multi-dipole ring cusp

C. M. Cooper, D. B. Weisberg, I. Khalzov, J. Milhone, K. Flanagan, E. Peterson, C. Wahl, and C. B. Forest

Citation: [Physics of Plasmas](#) **23**, 102505 (2016); doi: 10.1063/1.4963850

View online: <https://doi.org/10.1063/1.4963850>

View Table of Contents: <http://aip.scitation.org/toc/php/23/10>

Published by the [American Institute of Physics](#)

Articles you may be interested in

[Driving large magnetic Reynolds number flow in highly ionized, unmagnetized plasmas](#)

Physics of Plasmas **24**, 056502 (2017); 10.1063/1.4978889

[The Madison plasma dynamo experiment: A facility for studying laboratory plasma astrophysics](#)

Physics of Plasmas **21**, 013505 (2014); 10.1063/1.4861609

[Plasma confinement by localized cusps](#)

The Physics of Fluids **19**, 1045 (1976); 10.1063/1.861575

[Study on the structure and transition of the hollow plume in a multi-cusped field thruster](#)

Physics of Plasmas **23**, 103517 (2016); 10.1063/1.4965910

[Fully nonlinear \$\delta f\$ gyrokinetics for scrape-off layer parallel transport](#)

Physics of Plasmas **23**, 102302 (2016); 10.1063/1.4964666

[The nuclear size and mass effects on muonic hydrogen-like atoms embedded in Debye plasma](#)

Physics of Plasmas **23**, 103515 (2016); 10.1063/1.4965909



**COMPLETELY
REDESIGNED!**

**PHYSICS
TODAY**

Physics Today Buyer's Guide
Search with a purpose.

Direct measurement of the plasma loss width in an optimized, high ionization fraction, magnetic multi-dipole ring cusp

C. M. Cooper,^{1,2} D. B. Weisberg,^{2,3} I. Khalzov,^{2,4} J. Milhone,^{2,3} K. Flanagan,^{2,3}
 E. Peterson,^{2,3} C. Wahl,^{2,3} and C. B. Forest^{2,3}

¹Oak Ridge Associated Universities, Oak Ridge, Tennessee 37831, USA

²Center for Magnetic Self Organization, University of Wisconsin, Madison, Wisconsin 53706, USA

³Department of Physics, University of Wisconsin, Madison, Wisconsin 53706, USA

⁴Kurchatov Institute, Moscow, Russia

(Received 9 February 2016; accepted 19 September 2016; published online 17 October 2016)

The loss width of plasma in the WiPAL multi-dipole magnetic ring cusp [Cooper *et al.*, Phys. Plasmas **21**, 13505 (2014); Forest *et al.*, J. Plasma Phys. **81**, 345810501 (2015)] has been directly measured using a novel array of probes embedded in the insulating plasma limiters. The large plasma volume (~ 10 m³), small loss area associated with strong rare earth permanent magnets ($B_o \sim 2.23$ kG at face), and large heating power (≤ 200 kW) produces a broad range of electron temperatures ($2 < T_e < 15$ eV), ion temperatures ($0.03 < T_i < 2$ eV), plasma densities ($3 \times 10^{10} < n_e < 2 \times 10^{12}$ cm⁻³), and ionization fractions ($0.05 < n_e/(n_e + n_n) < 1$), in both argon and helium, all of which were accurately measured. This plasma regime, accessible with high magnetic fields, differs from previous devices: the cusp loss width is much larger than the Debye length and electron gyroradius and comparable to the collision length. Plasma parameters measured at the surface of ceramic limiter tiles covering the magnets and along radial chords in the cusp magnetic field indicate that electron density and temperature are nearly constant on magnetic field lines and that the mirror forces play little role in confining the plasma other than to constrict the loss area. Particle balance modeling is used to determine the cross field diffusion coefficient base on the measured losses to the limiters. The experimentally determined cross field diffusion coefficient (which determines the cusp loss width) is consistent with ambipolar diffusion across five orders of magnitude. The ambipolar diffusion across a given field line is set primarily by the electron-neutral collisions in the region where the magnetic field is the weakest, even though these plasmas can have ionization fractions near 1. *Published by AIP Publishing.*

[<http://dx.doi.org/10.1063/1.4963850>]

I. INTRODUCTION

Permanent magnet, multi-dipole cusps have long been used as a plasma confinement mechanism for a diverse set of applications, including hall thrusters,³ plasma processing machines,⁴ neutral beam heating sources,^{5,6} and basic plasma physics research experiments.⁷ They consist of rings of magnets with alternating ring to ring polarity. A multi-dipole magnetic field reduces plasma losses to a boundary by diverting plasma to the narrow regions where the magnetic fields intersect the wall, creating magnetic “bubbles” where no plasma is lost.⁸ The cusp magnetic field vanishes far away from the multi-dipole cusp leaving no magnetic field except those generated by external mechanisms.

Previous experiments measuring the cusp loss width developed empirical formulas by scaling single plasma parameters. Some are proportional to the ion gyroradius⁹ but the most widely reported loss width is proportional to the hybrid gyro-radius $w = 4\sqrt{\rho_e \rho_i}$,^{10,11} where $\rho_\alpha = v_\alpha/\omega_{c\alpha}$ and $\omega_{c\alpha} = eB/m_\alpha c$ is the cyclotron frequency for $\alpha = e, i$ electrons and ions. Several transport models have been developed to predict the cusp loss width $w = 2\sqrt{D_\perp L/c_s}$,^{6,12} assuming parallel losses along B . This depends on the cross field diffusion coefficient D_\perp and magnetic field line length L over which the plasma diffuses, where $c_s = \sqrt{k_B T_e/m_e}$ is

the plasma sound speed for the electron temperature T_e . This model shares similar plasma parameter scalings as the hybrid gyroradius prediction;¹³ however, it uses ill-defined fitting parameters B and L which can always be selected to fit the data over a small scaling.¹⁴ Ionization¹⁵ and geometric effects¹⁶ have been added to these models but a fully predictive model including magnetic topology to predict cusp widths is still lacking.

New manufacturing breakthroughs have yielded large, low cost, high field (> 3 kG) permanent magnets, which further reduce losses and improve confinement. This is coincident with a renewed interest in multi-dipole cusp confinement schemes for fusion,^{17–19} microdischarge thrusters,²⁰ and basic plasma research in regimes with higher temperature, density, and ionization fraction.^{1,21} Advances in numerical simulations have successfully captured some of the physics with kinetic modeling of the electron species but cannot directly simulate the experimental values achieved in the laboratory.⁵ Fluid models can be used to capture aspects of the transport but require experimental validation.

Recently, a large, magnetic multi-dipole confinement device in an axisymmetric ring cusp geometry has been constructed using the new generation of high field magnets (Fig. 1). The resulting plasma has an unprecedented particle confinement time (~ 1 – 5 ms) and ionization fractions close

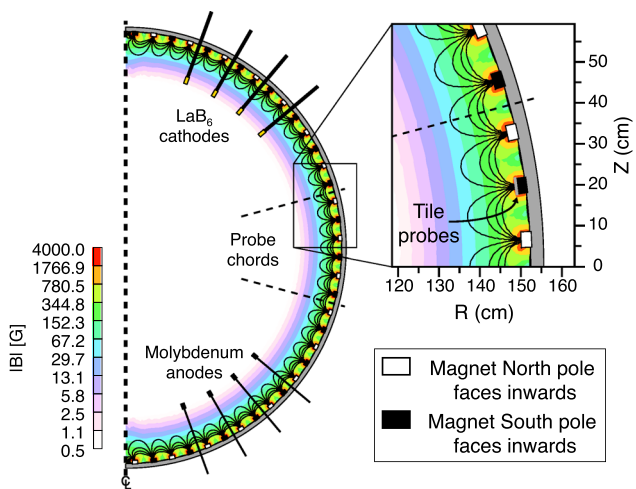


FIG. 1. A cutaway of the WiPAL vessel and the 36 multi-dipole, tile-covered magnet rings making up the cusp region, where the color denotes the magnetic field strength. A close up of the vessel edge shows the location of tile with Langmuir probes.

to 1.¹ This manuscript presents the first direct measurements of the cusp loss widths across a large scaling of plasma parameters (Fig. 3) in this new regime as well as a self consistent ambipolar theory to model the results. This model updates cusp loss theory and can be used to evaluate the loss widths in other magnetic cusp confinement devices. Section II describes the experimental setup of the device and Section III describes the cusp loss width measurements. The diffusive model is described in Section IV with the data agreeing well with an ambipolar diffusive model. Section V describes the coupled differential equations that can be solved in a generalized device to predict the cusp loss width given the magnet field geometry and the plasma parameters at the boundary of the cusp.

II. EXPERIMENTAL SETUP

The experiment is performed in the Wisconsin Plasma Astrophysics Laboratory (WiPAL) at the University of Wisconsin, Madison.^{1,2} A 1.5 m radius spherical vacuum vessel is evacuated and backfilled with a fill gas ($1 \times 10^{-5} - 10^{-4}$ Torr). Lanthanum Hexaboride (LaB_6) rods between magnet rings are heated until thermal emission and biased <400 V with respect to anodes, drawing <100 A of current each for <3 s, ionizing the fill gas. Confinement is provided by 36 axisymmetric rings of 2.23 kG magnets with alternating polarity spaced every 5 poloidal degrees (13.3 cm) on the outer surface of the sphere pointing radially inward. The resulting magnetic cusps are cylindrically symmetric in the toroidal direction but have a different toroidal length depending on its poloidal position. The different ring lengths do not affect the magnitude of the magnetic field at the surface of the tile or between magnet rings but subtly shift the magnetic center between the rings poloidally a few millimeters from the smallest to largest rings (see Fig. 1) and do not affect transport beyond a small correction. The multi-dipole cusp magnetic field drops below 1 G 0.3 m away from the wall leaving a 1.2 m radius unmagnetized volume.

Plasma produced in the unmagnetized volume drifts towards the walls where it is channeled into thin loss areas,

terminating on alumina insulating tiles 0.3 cm thick that cover the magnets. The total loss area along the alumina insulating tiles measured in this manuscript varies from $\sim 1000 - 4000 \text{ cm}^2$ depending on the measured cusp loss width. The loss area of the probes, anodes, and cathodes varies with insertion depth and number and is typically an additional $\sim 1000 - 2000 \text{ cm}^2$. Langmuir probes are swept in voltage and used to measure the electron temperature T_e , plasma potential Φ_p , and floating potential Φ_f using standard Langmuir probe techniques.²² The ion saturation current i_{sat} and electron saturation current e_{sat} of the probe are used to calculate the electron and ion flux to the surface of the probe $\Gamma_i = i_{sat}/e$ and $\Gamma_e = e_{sat}/e$, where e is the charge of an electron.²³ The electron density n_e is measured using a 1 mm microwave interferometer and the ion temperature is measured using a Fabry-Perot interferometer both imaging the homogenous unmagnetized core. The neutral density at the wall is measured with a cold cathode ion gauge.

The plasma parameters are consistently measured to be constant across the unmagnetized core for all experimental setups. This is supported by a simple radial transport model where plasma produced throughout the volume is lost through sheaths on the limiter tiles along the magnet rings and across the cusp loss width which cover $\sim 1\%$ of the surface area. Assuming plasma is lost through the sheaths at the plasma sound speed, flux conservation dictates that the radial flow just outside the magnetic cusps is $\sim 1\%$ the sound speed to within a geometric factor, too low to support any radial gradients in plasma parameters in the unmagnetized core. This applies to input power in the form of the electron beam from the LaB_6 cathodes. The thermal conductivity and particle mobility are too high to support gradients in plasma parameters due to non-local heating or ionization. However, radial gradients in the neutral gas have been observed through Abel inversions of neutral light (which indicates a hollow profile) compared to ion light (which indicates a constant profile). This too is consistent with the radial transport model: due to the high n_e and T_e , the mean free path of a neutral gas particle at the wall temperature can be as short as 20 cm in argon. However, the wall-measured neutral gas is an accurate approximation for the neutral gas density for the last few centimeters of plasma where the cross-field transport occurs and will be cited for the remainder of the paper.

III. CUSP LOSS WIDTH MEASUREMENTS

An array of twenty Langmuir probes measuring 0.01 cm by 0.25 cm are mounted on the surface of an insulating tile spaced 0.012 cm apart spanning from $-0.17 < x < 0.07$ cm across the loss region on the center of the 3.8 cm wide magnet at a poloidal angle $\theta = 102.5^\circ$, two rings south of the equator. The probes are arrayed along and across the magnet face with spatial redundancy to determine the location and orientation of the tile and probes and to prevent interference and improve the position uncertainty to 0.005 cm, the size of the dots in Fig. 2. Identical voltage sweeps are concurrently applied to measure profiles of the plasma parameters along the loss region. An example from a 75 kW discharge in a 1.3×10^{-5} Torr helium plasma is shown in Fig. 2. The plasma parameters

measured by a Langmuir probe in the homogenous unmagnetized core plasma ($r = 120$ cm) are plotted as dashed lines. The values of T_e , n_e , Φ_f , and $\Gamma_p = \Gamma_i$ measured in the core agree with the tile probes on the magnetic field lines which map to the core ($-0.02 < x < 0.02$ cm). This is typical of all experiments performed in this dataset and consistent with observations in other experiments of free-streaming plasma losses along the magnetic field at center of the magnetic rings. The only plasma parameter that changes along these field lines is the plasma potential Φ_p , indicating a large scale electric field in the cusp region. The electron gyroradius and Debye length ($\lambda_D = \sqrt{kT/4\pi n_e e^2}$) are both $\sim 1 \times 10^{-3}$ cm, much smaller than the probe justifying Langmuir curve

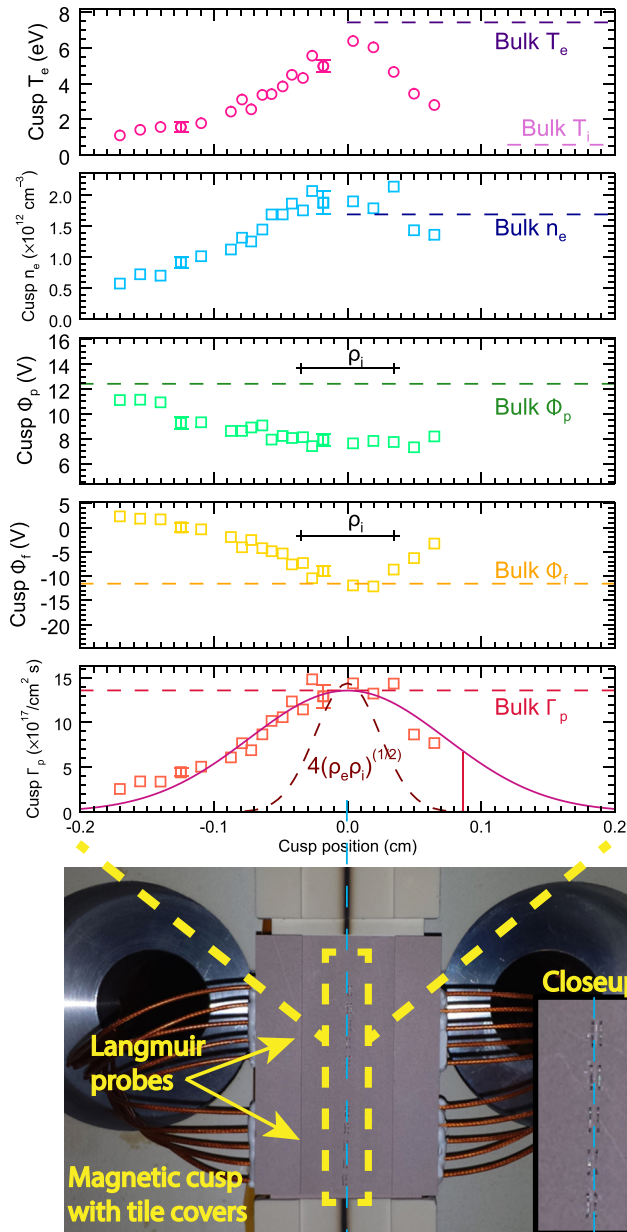


FIG. 2. (Top) Profiles of plasma parameters across the cusp loss region measured with the probes embedded in the tile terminating the plasma. Error bars indicate the accuracy of the measurement and the standard deviation over many sweeps. (Bottom) A picture of the tile with embedded probes upon installation. Deposition marks associated with the plasma footprint (i.e., the cusp loss width) can be seen on the older tiles above and below.

analysis and quasineutrality throughout the cusp region. The ion gyroradius at the wall is plotted. The empirical cusp loss width¹⁰ $w = 4\sqrt{\rho_e \rho_i}$ is plotted over the measured plasma flux to the wall with the measured width ~ 3 times larger. The plasma lost through the cusp loss width at the location of the tile is indicative of the loss on all the cusps since they have the same magnetic geometry and boundary conditions. Measurements of the deposition marks associated with the plasma footprint on the cusps made when servicing the device (i.e., the cusp loss width) vary less than 10% across all cusps, supporting the constant loss widths on all cusp rings.

The measurements of the cusp loss width are repeated over a scaling of input power and neutral fill density for helium and argon to investigate the scaling of the loss widths (Fig. 3(a)). The machine has a typical base pressure corresponding to a density of $\sim 1 \times 10^{10}$ cm⁻³ but as shown later in the paper, the cusp loss width depends on electron parameters and not ion or impurity ion parameters. The corresponding plasma parameters measured in the core are plotted in Figs. 3(b) and 3(d), demonstrating a large scaling. The profiles for the plasma lost to the wall, Γ_p , are fit to a Gaussian profile to establish a total particle loss rate and a characteristic full-width half-max. These measured widths are plotted in Fig. 3(c), as a function of the empirical prediction. There is no well established scaling and the measurements are multi-valued indicating a departure from previous experimental observations in this plasma regime. The cusp loss width scalings are similarly scattered and multi-valued when comparing to ρ_e , ρ_i , and diffusion widths¹² and in all cases disagree by an order of magnitude. It is possible to re-create a favorable scaling with any of the proposed loss widths by using a subset of only a few data points over a small scaling of a single plasma parameter; however, no large scale trends are clearly present from this dataset comprised of 182 unique plasma discharges over a large scaling of all plasma parameters.

IV. AMBIPOLAR CUSP TRANSPORT MODEL

The results of Fig. 3 motivate investigating a self-consistent plasma transport model by solving the plasma continuity equation in the magnetic cusp geometry. A cartoon of plasma transport between two magnet rings is shown in Fig. 4. The volume can be divided into two distinct regions, a weakly magnetized region far from the magnets where cross field mobility is highest and a strongly magnetized region close to the magnets where it is the lowest. The details are summarized in Table I. The cross field diffusion coefficient for both species is several orders of magnitude larger in the weakly magnetized region which is where most of the diffusion occurs. The cross field ion diffusion coefficient is typically an order of magnitude higher than the cross field electron diffusion coefficient throughout the region.

Plasma diffusion across the field, Γ_{\perp} , is balanced by losses where the field lines intersect the tile, Γ_{\parallel} , as well as any plasma sources due to ionization S_z ²⁴ or sinks due to radiative processes²⁵ and 3 body recombination²⁶ S_r in the volume. The total fueling rate is $S_p = S_z - S_r$ (though $S_r \ll S_z$ for WiPAL plasmas). The Langmuir probe measurements are made along two axes: radial probe measurements

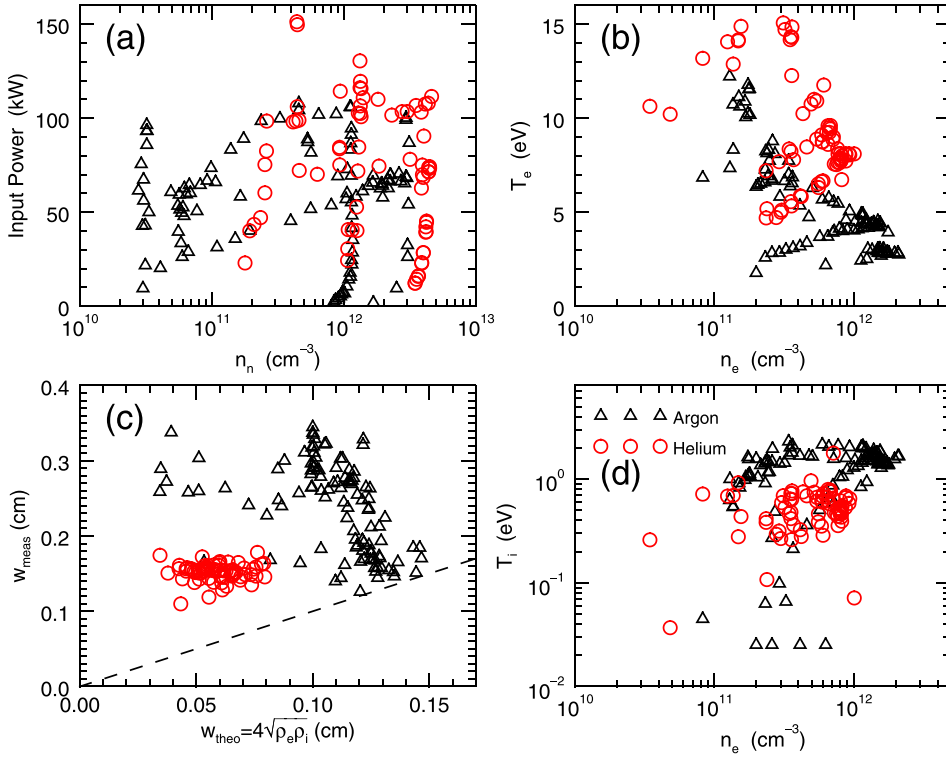


FIG. 3. (a) The experimental settings for the 182 cases in the scaling study and the resulting measured equilibrium values of (b) T_e , n_e , and (d) T_i in the WiPAL unmagnetized core. (c) The directly measured cusp loss width compared to a previous empirical model.

that bisect magnetic field lines at the local minimum in the magnetic field B_{min} (denoted as the \hat{y} direction), while tile measurements are made on the magnet surface at a local maximum in the magnetic field B_{max} (denoted as the \hat{x} direction). The cusp loss width (~ 0.1 cm) is much smaller than the magnet width (3.8 cm) so the magnetic field is assumed constant over the cusp loss width. This is confirmed by measurements and magneto-static simulations.

The rings closest to the equator, including the ring with the measurement tile, have a ring-to-ring change in ring diameter of only a few percent and the magnet faces on two adjacent rings are within a few degrees of anti-parallel. Since the ring radius is much larger than the ring-to-ring

spacing, the cusp magnetic field on these rings is well approximated using a Cartesian prescription. In the limit of negligible plasma current, the magnetic scalar potential ψ of the cusp magnetic field serves as a flux coordinate where $\nabla\psi \times \nabla p = 0$. In terms of ψ , l (the parameterized distance along a field line), and ξ (the distance normal to a field line), the particle continuity equation between two field lines at ψ and at $\psi + \Delta\psi$ is

$$\int [\Gamma_{\perp}(\psi) - \Gamma_{\perp}(\psi + \Delta\psi)] dl = 2\Gamma_{\parallel}\Delta x - \int S_p \Delta\xi dl, \quad (1)$$

where Δx is the width of the parallel flux channel that is lost to the magnet face, $\Delta\xi dl$ is the differential area bounded by the two field lines, and the particle source rate $S_p = S_z - S_r$ is constant along flux surfaces. The expression in Eq. (1) is the Cartesian approximation to the cusp region valid for the large radius and high multi-dipole moment of WiPAL, invariant in the coordinate into the page which cancels out of

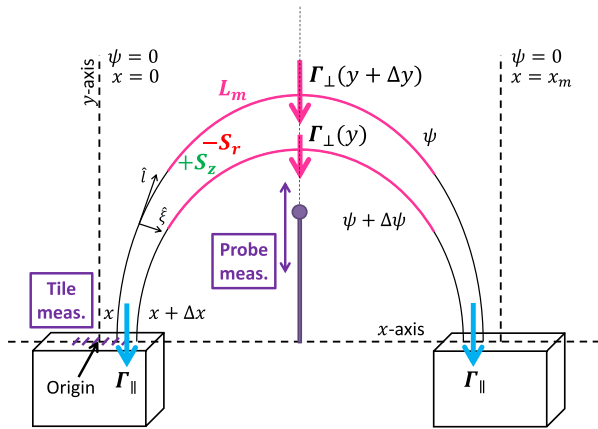


FIG. 4. A cartoon of the 1D transport processes in the cusp region. Particle flux across the magnetic field far away from the magnets is balanced by the losses along the field lines at the tiles subject to sources due to ionization and losses due to recombination. The locations of the Langmuir probe measurements and the tile measurements are shown.

TABLE I. List of plasma parameters related to magnetization and diffusivity for the low field, high diffusion region between magnet rings and the high field, low diffusion region near the magnet rings. The ranges represent the spread in the data $\mu = [4, 40]$, $10^{11} < n_e < 10^{12}$ cm^{-3} , $10^{10} < n_n < 10^{12}$ cm^{-3} , $1.5 < T_e < 15$ eV, $0.2 < T_i < 2$ eV.

WiPAL cusp region	Low field	High field
B (g)	10^1	10^3
ω_{ce} (s^{-1})	10^7	10^{10}
ω_{ci} (s^{-1})	$10^3 - 10^4$	$10^5 - 10^6$
ν_{en} (s^{-1})	$10^4 - 10^6$	$10^4 - 10^6$
ν_{in} (s^{-1})	$10^1 - 10^3$	$10^1 - 10^3$
$D_{e,\perp}$ ($\text{cm}^2 \text{s}^{-1}$)	$10^3 - 10^6$	$10^{-2} - 10^2$
$D_{i,\perp}$ ($\text{cm}^2 \text{s}^{-1}$)	$10^4 - 10^7$	$10^{-1} - 10^3$

every term. Expressing the line integrated cross-field flux as a flux-averaged quantity allows the definition of a characteristic length L_m

$$\int \Gamma_{\perp} dl = \langle \Gamma_{\perp} B \rangle \int \frac{dl}{B} \equiv \langle \Gamma_{\perp} B \rangle \frac{L_m}{B_{min}}, \quad (2)$$

where L_m is the width along the field line of the region of largest cross-field flux, which occurs primarily near the middle of the field line far from the magnets where the magnetic field is at a minimum. Using the flux coordinate identities

$$\begin{aligned} B(\psi, l) &= \Delta\psi / \Delta\xi, \\ B_{max} &= \Delta\psi / \Delta x, \\ B_{min} &= \Delta\psi / \Delta y, \end{aligned}$$

and assuming most of the diffusion occurs along a region of length L_m , the continuity equation can be written in differential form as

$$\frac{d\Gamma_{\perp}}{dy} = -\frac{2\Gamma_{\parallel}}{L_m} \frac{B}{B_{max}} + S_p. \quad (3)$$

In a multi-dipole magnetic cusp geometry, B decays exponentially in the \hat{y} direction, and a coordinate transform between the position on the magnet face x and probe position y is derived from the magnetic flux geometry. To a good approximation only the lowest Fourier components of the magnetic field can be used so that

$$\frac{\partial x}{\partial y} = \frac{B_{min}}{B_{max}} = e^{-k_x y}, \quad k_x = \frac{\pi}{x_m}. \quad (4)$$

The coordinate transformation described by Eq. (4) is used to compare measurements of plasma parameters along a field line. T_e and n_e measured at the surface of the tile and their Gaussian fits for a helium plasma with $n_n = 1.2 \times 10^{12} \text{ cm}^{-3}$ are transformed using Eq. (4) and plotted as a function of WiPAL radius $r \equiv r_m - y$ where r_m is the radius of the surface of the tile covering the magnet, 149.9 cm. Local measurements from a separate Langmuir probe along this chord bisecting the two magnet rings (location shown in Fig. 4) are plotted in Fig. 5. This amounts to measuring the plasma parameters in the middle and end of the same field line. Since the magnet rings are nearly the same radius and anti-parallel, the physical center of the rings is coincident with the magnetic center of the rings. The probe measurements bisecting the rings are along the magnetic center and shifting the probe data using the coordinate transformation is well motivated. For the rings closer to the poles, there is a larger shift in ring radius and the magnetic center may shift towards the poles a few millimeters, about the width of the Langmuir probe used to measure plasma parameters between magnet rings (see Fig. 4). All the plasma parameters except the plasma potential are constant along magnetic field lines in the cusp region consistent with high plasma mobility along the magnetic field and low mobility across it. The change in plasma potential indicates a large scale electric field in the cusp region along and across magnetic field lines (Fig. 5(b)). The overlapping measurements are confirmed for

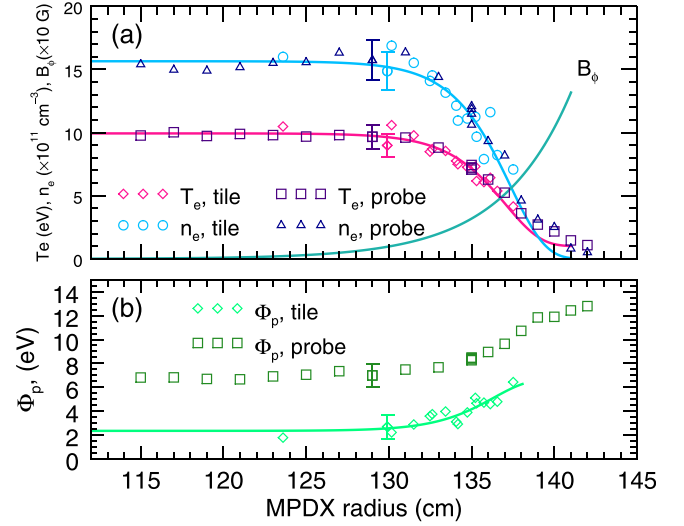


FIG. 5. (a) The tile measurements of T_e and n_e and their Gaussian fits transformed by Eq. (4) and plotted as a function of WiPAL radius. These are in agreement with local Langmuir probe measurements on the same magnetic field line in the gap between magnets indicating that plasma parameters are constant along field lines. (b) The plasma potential from the tile and probe measurements in the same geometry. The difference in the measurements indicates the presence of a large scale electric field in the cusp region along and across the magnetic field lines.

several cases and the tile measurements can be transformed along y and used to calculate S_p , evaluate Eq. (1) and compare to theoretical predictions.

A second detail for establishing the transport model is the relative particle flux rates in the cusp region. The plasma strike point on the magnet is covered by an insulating tile which prevents charge from flowing between the field lines and short-circuiting the plasma. This enforces a charge neutral flux to the wall in steady state, enforced by self-consistently formed sheaths on the tile. The magnitude and sign of the sheath potential measured by the probes, Φ_f , are consistent with these observations. There are no measurable differences in the shapes of the normalized particle flux profiles to the wall, further supporting charge neutral transport rates throughout the cusp region and implying $\vec{\Gamma}_e = \vec{\Gamma}_i = \vec{\Gamma}$. Finally, the perpendicular electric field points inward, which is attributed to an ambipolar electric field set by the ion mobility being larger than the electron mobility. Interestingly, since the cusps terminate on insulators, there is no absolute plasma potential established by the cusp losses. The plasma carries a diffuse current across the anodes and cathodes, which affects the plasma sheaths on the individual components. The anodes are tied to ground through a 1 k Ω resistor, so the anode sheath sets the plasma potential. The cathode sheath develops self consistently based on the anode cathode bias, the cathode emissivity, the relative surface areas, and plasma conditions. The cusp insulator sheaths have a fixed potential drop to enforce the current free system, so the insulator surface potential boundary condition changes to accommodate the plasma potential. Further details of the system will be published in an upcoming manuscript.

The probes in the tile provide a direct measurement of $\Gamma_{\parallel}(x)$ and through the coordinate transform provide $n_e(y)$

and $T_e(y)$. The right hand side of Eq. (3) is evaluated numerically to calculate the rate of change of the cross field flux, $\partial\Gamma_{\perp}/\partial y$. An example calculation for a helium plasma with $T_e = 7.8$ eV, $n_e = 8.1 \times 10^{11}$ cm $^{-3}$, and $n_n = 4.5 \times 10^{12}$ cm $^{-3}$ is plotted in Fig. 6(a). Eq. (3) is integrated to calculate the cross field particle flux $\Gamma_{\perp}(y)$ by enforcing $\Gamma_{\perp} = 0$ at $y=0$, shown in Fig. 6(b). The profile peaks due to the geometric effects and the presence of ionization. This is the indirectly measured cross field flux that self consistently describes the losses at the wall using particle conservation; no plasma physics transport coefficients have been used.

An ambipolar diffusion model including neutral particle collisions is used to model the transport

$$\Gamma_{\perp} = -D_{\perp,n_e}\nabla_{\perp}n_e - \frac{n_e}{T_e}D_{\perp,T_e}\nabla_{\perp}T_e = -D_{\perp,e}\frac{\partial n_e}{\partial y}, \quad (5)$$

where

$$D_{\perp,e} = \frac{k_B T_e \nu_e}{m_e (\nu_e^2 + \omega_{ce}^2)} \left(1 + \frac{(n_e \partial T_e / \partial y)}{(T_e \partial n_e / \partial y)} \right) \quad (6)$$

is the diffusion coefficient in the presence of temperature and density gradients and $\nu_e = n_n \sigma_n \nu_e$ is the electron neutral collision frequency for a neutral particle with cross sectional area $\sigma_n \sim 5 \times 10^{-15}$ cm 2 . The quantity $D_{\perp,meas}$ is calculated from the data using Eq. (5)

$$D_{\perp,meas} \equiv -\frac{\Gamma_{\perp,meas}}{(\partial n_e / \partial y)}, \quad (7)$$

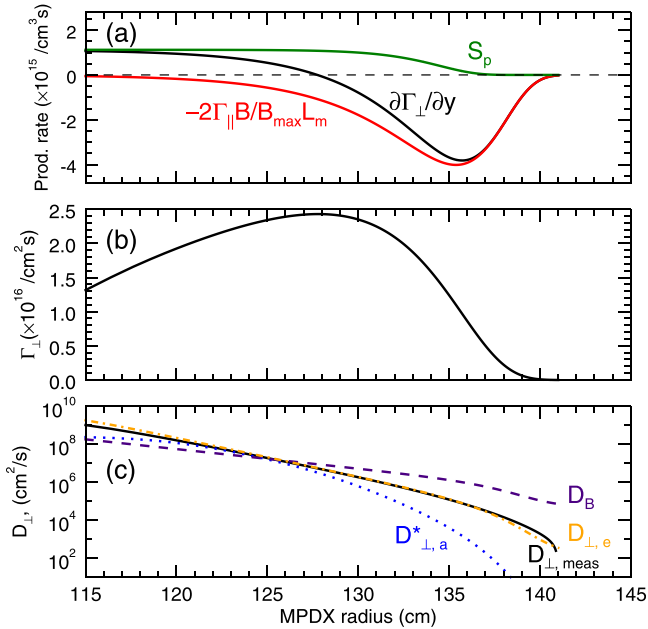


FIG. 6. (a) The terms in Eq. (1) evaluated along the plasma boundary between two rings in terms of the total particles per volume per second added from ionization (green) and lost at the wall (red) which sum to the change in the cross field flux (black). (b) The profile of the cross field flux found by integrating the profile in (a). (c) The profile of the corresponding diffusion coefficient from a diffusion model compared to profiles of several theoretical diffusion coefficients.

and is compared to Bohm diffusion D_B , cross field electron diffusion $D_{\perp,e}$, and an ambipolar diffusion model corrected for low magnetic field²⁷ $D_{\perp,a}^*$ in Fig. 6(c). In the ambipolar model, an electric field forms to regulate the relative transport rates of the two species, maintaining a current free system. As seen in Table I, $D_{\perp,i} > D_{\perp,e}$ throughout the cusp region so the electric field merely reduces ion transport to match the electron transport and $D_{\perp,a} \sim D_{\perp,e}$ for both species. Modifications to the electric field due to the magnetic cusp only modify the ion transport and can be ignored for the total current-free transport which happens at the electron diffusion rate. Excellent agreement is found with the ambipolar model in the electron diffusion limit. The other models agree with the measurements at single locations but do not agree across the entire boundary. Previous 0D models can be scaled to match these other diffusion rates at one point but only the ambipolar model exhibits large scale agreement across the entire 1D profile, which this letter is the first to measure. A value of $L_m = 6$ cm fits the data best and is consistent with the physical setup considering that most of the diffusion occurs over the length of the field line farthest from the magnets spaced $x_m = 13.3$ cm apart. Eq. (2) is evaluated numerically and found to slowly vary from 8.3–8.4 cm along the 1D transport profile in the cusp region with $L_m = 8.4$ cm at the point of largest cross field flux (i.e., $r = 127$ cm for the case in Fig. 6). This calculation confirms the left hand side of the model in Eq. (1) and agrees reasonably well with the fits to the data given the assumptions. In future models, the terms will all be calculated individually since the two line integrals have different values of L_m in the 2D limit.

The value of $D_{\perp,meas}$ is compared to $D_{\perp,e}$ at the point of largest cross field flux (i.e., $r = 127$ cm for the case in Fig. 6)

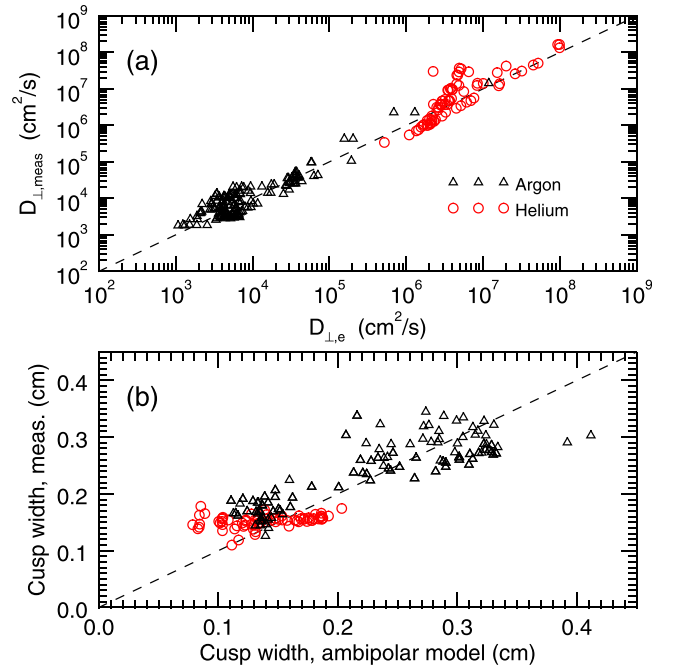


FIG. 7. The scaling of the effective diffusion coefficient calculated from the measured plasma parameter profiles evaluated at the point of highest cross-field flux for all 182 shots, and the corresponding theoretical ambipolar coefficient calculated at the same point.

for each discharge in the dataset and shown in Fig. 7(a). The parameter scan produces a very large scaling in predicted ambipolar coefficient and the data agree with the predictions very well for $L_m = 6$ cm in helium and $L_m = 20$ cm in argon, indicating that the measured cross field diffusion rates in argon may be 3 times higher than the electron diffusion rate. The data trend slightly away from the theoretical line possibly due to modifications of the predicted ambipolar rates. For some experiments, T_i is comparable to T_e and the electric field increases the cross field electron transport as much as a factor of 2, which would double the theoretical calculation of $D_{\perp,e}$ bringing the data to the right, closer to the predicted line and double L_m . However, the electric field in the cusp region between the rings could not be measured for the scaling and its small effects on the transport cannot be included in the analysis. In some argon discharges, the particle confinement time is sufficiently long (<5 ms) and T_e is sufficiently high that a comparable density of Ar^{+2} and Ar^{+3} ions can be present, further changing the transport rate predictions. The typical $D_{\perp,meas}$ in argon is lower than in helium due to the lower T_e (limited by radiation) and lower n_n (from the lower ionization energy) for these experiments, consistent with the ambipolar model where cross field electron transport limits the plasma transport. If the cross field diffusion was a result of ion physics, the observed rates for argon would be an order of magnitude higher than helium for similar plasma parameters. Similarly, the measured rates would be comparable for the two species for Bohm diffusion independent of n_n .

V. CUSP LOSS WIDTH PREDICTION USING AMBIPOLAR DIFFUSION MODEL

As a final test of the model, the 1D ambipolar transport rates are evaluated numerically to predict the cusp loss widths using only the core plasma parameters. The second order transport differential equation is formulated into two normalized first order differential equations to simultaneously solve for $n_e(y)$ (as described by Eq. (5)) and $\Gamma_{\perp}(y)$ (as described by Eq. (1)) along the region of high cross field diffusion $x = x_m/2$

$$\frac{\partial \bar{n}_e(\bar{y})}{\partial \bar{y}} = -\frac{\bar{\Gamma}_{\perp}(\bar{y})}{\bar{D}_{\perp,e}(\bar{y})}, \quad (8)$$

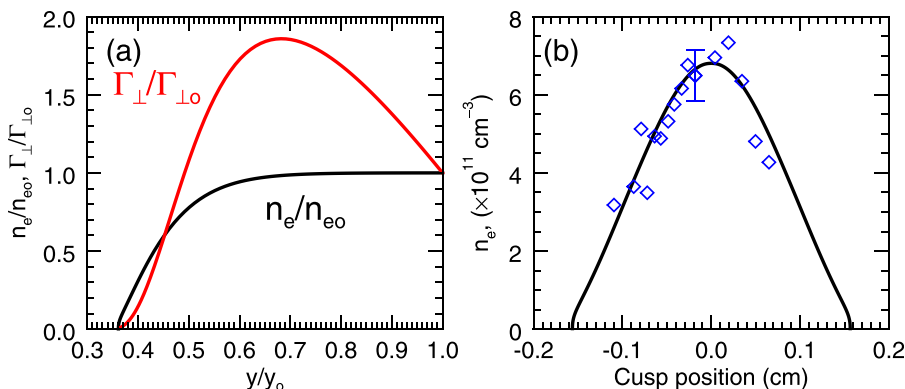


FIG. 8. (a) Profiles for the normalized quantities $\bar{n}_e(\bar{y})$ and $\bar{\Gamma}_{\perp}(\bar{y})$ as described by Eq. (9). The initial position occurs at $\bar{y} = 1$ and solves towards $\bar{y} = 0$. (b) The profile in graph (a) transformed into the cusp ring coordinates and compared to measurements on the tile face. This simulation corresponds to the same case in Fig. 5.

$$\frac{\partial \bar{\Gamma}_{\perp}(\bar{y})}{\partial \bar{y}} = -\frac{\bar{\Gamma}_{\parallel}(\bar{y})}{L_m} + \bar{S}_p(\bar{y}), \quad (9)$$

where \bar{n}_e , $\bar{\Gamma}_{\perp}$, and \bar{y} are quantities normalized to the initial core density n_{eo} , cross field flux $\Gamma_{\perp 0}$, and a system length L , respectively. The equations are solved using a variable-stepsize fourth order Runge Kutta solver. In addition to checking for local agreement with the ambipolar model (Fig. 7(a)), this calculation confirms the global legitimacy of the ambipolar model while establishing a set of equations that can be extended to any experimental device to predict the loss width.

To compare to the experiment, the solver uses the values of n_e , T_e , and T_i measured in the core of WiPAL and n_n , measured by the cold cathode ion gauge as the initial conditions and solves the transport equations from $r \sim 120$ cm (defined as $\bar{y} = 1$ with $\bar{y} = 0$ corresponding to the WiPAL vessel wall) outward until $\bar{n}_e(\bar{y}_f) = 0$. The initial value of r is chosen to be as far away from the wall as possible but still close enough to be able to ignore spherical effects. The initial value of $\Gamma_{\perp 0}$ is not known (i.e., the initial value of $\partial n_e/\partial y$) so it is varied until the criterion $\bar{\Gamma}_{\perp}(\bar{y}_f) = 0$ is coincident with $\bar{n}_e(\bar{y}_f) = 0$ for the same \bar{y}_f using a shooting method. This corresponds to the cross field flux and the density going to 0 at the same location, consistent with the experiment and physical intuition. In order to capture the contribution of the changing value of T_e in the cusp region, a value of $T_e(y) = T_{eo}n_e(y)/n_{eo}$ is used, making the T_e profile the same shape as the n_e profile. As seen in Figs. 2 and 5, the two profiles are similar although measured widths of T_e and n_e vary $<20\%$. This effectively adds a factor of 2 to the diffusion coefficient and prevents having to self consistently solve the heat equation for the electrons. The loss to the walls is assumed to be a Bohm sheath, $\Gamma_{\parallel}(\bar{y}) = 0.62c_s(\bar{y})n_e(\bar{y})$. The 1D calculation extends work on recent 0D models⁶ and allows the loss width to be calculated given neutral fill pressure n_n , bulk plasma parameters T_{eo} , n_{eo} , and T_i , and the magnetic field $B(y)$. An example calculation is shown in Fig. 8(a).

The variables are transformed along the field lines using Eq. (4) to calculate $n_e(x)$, $T_e(x)$, $\Gamma_{\parallel}(x)$ along the surface of the magnets. An example profile is shown in Fig. 8(b) where the transformed simulation profile agrees very well with the data. The full-width half-max of the loss footprint is calculated to determine the loss width for the ambipolar model. The results are shown in Fig. 7(b). The predicted cusp widths agree well with the measured values. As a next step, this 1D

model can be expanded into a fully 2D model with varying neutral density due to ionization and several ion species and charge states.

VI. CONCLUSIONS

In summary, the loss widths of plasma terminating on an insulating tile in a multi-dipole magnetic cusp are measured across a scaling of T_e , T_i , n_e , n_n , and m_i of over an order of magnitude each. The cusp magnetic field is provided by rings of permanent magnets and static for these experiments. The particle transport is as follows. Bulk ionization produces plasma in the WiPAL core which is largely confined by the cusp magnetic field. The magnetic field limits cross-field diffusion and plasma is primarily lost parallel to the magnetic field where the field lines map to the magnet tile across the cusp loss width. Additional field lines along the plasma edge are populated via ambipolar cross-field diffusion due to plasma-neutral gas collisions, increasing the cusp loss width.

The majority of this cross field diffusion occurs where the magnetic field is the weakest along a field line, farthest from the magnets, and is proportional to the magnitude of the field and the edge density gradient at this location. For the parameters of this experiment, the ions diffuse more rapidly than the electrons across the field such that an ambipolar electric field develops to reduce cross field ion diffusion and enhance the electron losses. This creates a current-free system as required by the insulating boundary conditions (Fig. 2(c)). Thus, the losses are set by the cross field electron diffusion rate (Fig. 6(a)). A 1D plasma continuity model is developed in the cusp geometry to determine the cross field plasma flux and estimate an effective diffusion coefficient. The estimated diffusion coefficients are consistent with ambipolar diffusion over five orders of magnitude across a large region of the cusp and a large scaling of experimental parameters. A 1D ambipolar model is developed and solved numerically using the bulk plasma parameters as initial conditions and predicts the cusp loss width with good agreement.

These experiments raise a number of questions. Is there a discrepancy with previous results and if so, is it because these plasmas are more fully ionized? Can the plasma be better optimized by changing the magnet geometry (i.e., moving the rings closer or further apart)? More rings lead to additional loss area, but spreading the rings apart further decreases the magnetic field at the low field point near the plasma where a majority of the cross field diffusion occurs.

ACKNOWLEDGMENTS

This work was funded in part by NSF Award No. PHY 0821899, PFC Center for Magnetic Self Organization in Laboratory and Astrophysical Plasmas, and DOE.

- ¹C. M. Cooper, J. Wallace, M. Brookhart, M. Clark, C. Collins, W. X. Ding, K. Flanagan, I. Khalzov, Y. Li, J. Milhone *et al.*, *Phys. Plasmas* **21**, 13505 (2014), ISSN 1070-664X, 1310.8637.
- ²C. B. Forest, K. Flanagan, M. Brookhart, M. Clark, C. M. Cooper, V. Desangles, J. Egedal, D. Endrizzi, I. V. Khalzov, H. Li *et al.*, *J. Plasma Phys.* **81**, 345810501 (2015).
- ³R. Wirz and D. Goebel, *Plasma Sources Sci. Technol.* **17**, 035010 (2008), ISSN 0963-0252.
- ⁴P. Ventzek, R. Hoekstra, and M. Kushner, *J. Vac. Sci. Technol. B* **12**, 461 (1994).
- ⁵A. Hatayama, T. Shibata, S. Nishioka, M. Ohta, M. Yasumoto, K. Nishida, T. Yamamoto, K. Miyamoto, A. Fukano, and T. Mizuno, *Rev. Sci. Instrum.* **85**, 02A510 (2014), ISSN 1089-7623.
- ⁶T. Morishita, M. Ogasawara, and A. Hatayama, *Rev. Sci. Instrum.* **69**, 968 (1998), ISSN 00346748.
- ⁷R. Limpaecher and K. R. MacKenzie, *Rev. Sci. Instrum.* **44**, 726 (1973), ISSN 00346748.
- ⁸M. Haines, *Nucl. Fusion* **17**, 811 (1977), ISSN 0029-5515.
- ⁹R. Pechacek, J. Greig, M. Raleigh, D. Koopman, and A. Desilva, *Phys. Rev. Lett.* **45**, 256 (1980).
- ¹⁰N. Hershkovitz, K. Leung, and T. Romessert, *Phys. Rev. Lett.* **35**, 277 (1975).
- ¹¹K. Leung, N. Hershkovitz, and K. Mackenzie, *Phys. Fluids* **19**, 1045 (1976).
- ¹²R. A. Bosch and R. L. Merlino, *Phys. Fluids* **29**, 1998 (1986).
- ¹³A. Fukano, T. Mizuno, a. Hatayama, and M. Ogasawara, *Rev. Sci. Instrum.* **77**, 03A524 (2006), ISSN 00346748.
- ¹⁴A. Kumar and V. Senecha, *AIP conf. Proc.* **1390**, 150 (2011).
- ¹⁵C. Gauthereau and G. Matthieussent, *Phys. Lett. A* **102**, 231 (1984), ISSN 03759601.
- ¹⁶C. Gauthereau, G. Matthieussent, J. Rauch, and J. Godiot, *Phys. Lett. A* **101**, 394 (1984), ISSN 03759601.
- ¹⁷N. A. Krall, *Fusion Technol.* **22**, 9 (1992), ISSN 07481896.
- ¹⁸T. McGuire, *Magnetic Field Plasma Confinement for Compact Fusion Power*, U.S. patent no. US20140301518 A1 (2014).
- ¹⁹T. Dolan, *Plasma Phys. Controlled Fusion* **36**, 1539 (1994).
- ²⁰B. Dankongkakul, S. J. Araki, and R. E. Wirz, *Phys. Plasmas* **21**, 043506 (2014), ISSN 1070-664X.
- ²¹C. Collins, N. Katz, J. Wallace, J. Jara-Almonte, I. Reese, E. Zweibel, and C. Forest, *Phys. Rev. Lett.* **108**, 115001 (2012), ISSN 0031-9007.
- ²²I. Hutchinson, *Principles of Plasma Diagnostics* (Cambridge, 2002).
- ²³P. C. Stangeby, *Phys. Fluids* **27**, 682 (1984), ISSN 00319171.
- ²⁴D. Whyte, T. Evans, A. Kellman, D. Humphreys, A. Hyatt, T. Jernigan, R. Lee, S. Luckhardt, P. Parks, and M. Schaffer, in *Proceedings of the 24th European Conference on Controlled Fusion and Plasma Physics* (1997), Vol. 21A, p. 1137.
- ²⁵R. McWhirter, *Plasma Diagnostic Technologies* (Academic Press, New York, 1965).
- ²⁶Y. Zeldovich and Y. Raizer, *Physics of Shock Waves and High-Temperature Hydrodynamic Phenomena* (Academic Press, New York, 1966).
- ²⁷O. Olson and H. Skarsgard, *Can. J. Phys.* **43**, 855 (1965).